Core level shifts as indicators of Cr chemistry on hydroxylated α-Al2O3(0001): a combined photoemission and first-principles study†

Maya Messaykeh, Stéphane Chenot, Pascal David, Gregory Cabailh, Jacques Jupille, Alexey Koltsov, Pierre Lagarde, Nicolas Trcera, Jacek Goniakowski, Rémi Lazzari

▶ To cite this version:

Maya Messaykeh, Stéphane Chenot, Pascal David, Gregory Cabailh, Jacques Jupille, et al.. Core level shifts as indicators of Cr chemistry on hydroxylated α-Al2O3(0001): a combined photoemission and first-principles study†. Physical Chemistry Chemical Physics, 2021, 10.1039/D1CP03224K. hal-03359564

HAL Id: hal-03359564
https://hal.sorbonne-universite.fr/hal-03359564v1

Submitted on 30 Sep 2021

HAL is a multi-disciplinary open access archive for the deposit and dissemination of scientific research documents, whether they are published or not. The documents may come from teaching and research institutions in France or abroad, or from public or private research centers.

L'archive ouverte pluridisciplinaire **HAL**, est destinée au dépôt et à la diffusion de documents scientifiques de niveau recherche, publiés ou non, émanant des établissements d'enseignement et de recherche français ou étrangers, des laboratoires publics ou privés.

Journal Name

ARTICLE TYPE

Cite this: DOI: 00.0000/xxxxxxxxxx

Core level shifts as indicators of Cr chemistry on hydroxylated α-Al$_2$O$_3$(0001): a combined photoemission and first-principles study

Maya Messaykeh,[a] Stéphane Chenot,[a] Pascal David,[a] Gregory Cabailh,[a] Jacques Jupille,[a] Alexey Koltsov,[b] Pierre Lagarde,[c] Nicolas Trcera,[c] Jacek Goniakowski,[a] and Rémi Lazzari*[a]

Received Date
Accepted Date

DOI: 00.0000/xxxxxxxxxx

The Cr/α-Al$_2$O$_3$(0001) interface has been explored by X-ray photoemission spectroscopy, X-ray absorption spectroscopy (XAS) and *ab initio* first-principle calculations of core level shifts including final state effects. After an initial oxidation via a reaction with residual surface OH but no reduction of the alumina substrate, Cr grows in a metallic form without any chemical effect on the initially oxidized Cr. However, Cr metal lacks crystallinity. Long-range (reflection high energy electron diffraction) and short-range (XAS) order are hardly observed. Photoemission combined with atomistic simulations becomes a unique tool to explore chemistry and environment at the Cr/alumina interface. Cr 2p, O 1s and Al 2s shifted components are all explained by the formation of moieties involving Cr^{3+} and/or Cr^{4+} and of metallic Cr^0, which supports the previously found Cr buffer mechanism for poorly adhesive metals. Beyond the situation under study, the present data demonstrate the ability of a combined experimental and theoretical approach of core-level shifts to exhaustively describe the general case of disordered metal/oxide interfaces.

1 Introduction

Dielectric-supported films of late transition or coinage metals (Cu, Zn, Ag, Pt, Au) are encountered in many applications for their specific optical[1–5], electric[6,7], electronic[5,8] and catalytic[9,10] properties. Yet, a constant concern is the poor wetting at the metal/dielectric interfaces[11,12] which, even in the case of a sizeable coverage reached through kinetic effects, leads to the synthesis of inherently out-of-equilibrium films[13–16]. Layer stacks stable under operating conditions are commonly obtained through the pre-deposition of intermediate layers of early transition metals, the so-called buffers, such as Ni[1,17], Ti[2,4,5,8,18], Nb[1,19] and Cr[1,2,4,5,7]. In particular, we have focused in the recent years on the capacity of pre-deposited Cr to enhance the sticking, spreading and adhesion of Zn on α-Al$_2$O$_3$(0001)[20–25]. The subject was inspired by advanced high strength steels which are alloyed with electropositive elements (including aluminium) and used to lighten car weight to comply with energy saving rules. A shortcoming is that the corresponding steel grades are difficult to galvanize[26,27] because, due to oxygen-induced segregation, steel sheets are covered with oxides (in particular alumina[28–30]) at the end of cold rolling and recrystallization annealing. In such a context, the Zn/Cr/α-Al$_2$O$_3$(0001) model stack is of general relevance for the study of the mechanisms at work in the buffer effect. Chromium[1,2,4,7] is representative of the class of the early transition metals often encountered in buffers and α-Al$_2$O$_3$(0001) is an archetypal non reducible oxide surface[8,10,18,19,31,32]. In addition, in the conditions used herein, at 300 K in vacuum, Zn does not stick at all on bare alumina which eliminates any ambiguity as to the buffer effect.

The way Cr acts as a promoter for Zn sticking on alumina deserves attention. In the submonolayer range, Cr behaves as a very effective seed layer as minute metallic Cr amounts dramatically increase Zn sticking[25]. For example, a Cr coverage of $\sim 5\%$ allows the sticking of almost an entire dose of 15 Å of Zn[25]. Three-dimensional supported clusters, obtained commonly for transition metals on alumina or silica[11,12] as demonstrated for Cr/alumina by optics[25] and calculations[21,22], unexpectedly become effective buffers. The mechanism contrasts starkly with the common view of buffers as continuous two-dimensional layers. Beyond a clear academic interest, such a mechanism[25]

---

[a] *CNRS/Sorbonne Université, Institut des NanoSciences de Paris, UMR 7588, 4 Place Jussieu, F-75005 Paris, France*
[b] *ArcelorMittal Maizières Research, voie Romaine, F-57280 Maizières-lès-Metz, France*
[c] *Synchrotron SOLEIL, L'Orme des Merisiers, Saint-Aubin, BP 48, F-91192 Gif-sur-Yvette, France*
∗ Corresponding author: remi.lazzari@insp.jussieu.fr

† Electronic Supplementary Information (ESI) available: [Complementary figures of photoemission analysis of O 1s and Cr 2p core levels are given in ESI.]. See DOI: 00.0000/00000000.

is of prime importance in relation to applications in which (i) technical constraints exclude continuous buffer layers[1] or (ii) keeping properties of the functional layer requires reducing the buffer thickness as much as possible[1,5]. Because the extraordinary promotion of Zn sticking by minute Cr clusters relies on Zn attachment to metallic Cr[25], the interfacial chemistry plays a pivotal role in the process. Cr clusters are not entirely metallic. X-ray absorption spectroscopy (XAS) combined with first principles Density Functional Theory (DFT) calculations showed that, at the onset of its deposition, Cr reacts with residual OH groups[24] to mainly form Cr^{3+}-O_2H surface moieties while Cr does not reduce the alumina substrate[24]. However, the observation of reduced Al at the Cr/$\alpha-Al_2O_2(\bar{1}012)$ interface[33,34] or of oxidizied Cr on OH-free alumina thin film on NiAl(110)[35,36] question this finding. As the Cr film thickens, XAS[24] and UV-visible plasmonics[25] reveal a metallic behaviour but, in the absence of quantitative data, the frontier between the two media remains unclear. In particular, the formation of intermediate oxidation states at the Cr/Cr-O_2H interface cannot be excluded.

To establish on which chemistry the Zn/Cr/Al_2O_3 seed mechanism is relying, the present work aims at analysing all the elements involved at the Cr/α-Al_2O_3(0001) interface by photoemission. A comprehensive analysis of the Cr 2p, O 1s and Al 2s core level shifts is performed, including those induced by the contact at the metal/oxide interface in the absence of any chemical bond. Film crystallinity and ordering are analysed via XAS oscillations at the Cr K-edge and electron diffraction. In an original way, photoemission data are supplemented by *ab initio* calculations of core-level shifts prior to checking the consistency of the findings with the previous analysis of the same system[24,25].

2 Methods

2.1 Experimental

X-ray photoemission spectroscopy (XPS) was performed in an ultra-high vacuum (UHV) vessel composed of a preparation (base pressure of 2.10^{-10} mbar) and an analysis chamber (5.10^{-11} mbar)[25]. XPS was recorded under Al-Kα or Mg-Kα non-monochromatic excitation with an hemispherical analyser (Phoibos 100 from SPECS; delay line detector) at a pass energy of 20 eV or 50 eV in a normal emission configuration. No charge compensation was applied. Spectra were referenced to tabulated Al 2s binding energy (E_B) in Al_2O_3 ($E_B = 119.6$ eV)[37]. Film thicknesses were estimated by taking the ratio of substrate (O 1s and Al 2s) and deposit (Cr 2p) core level areas obtained after subtraction of a Tougaard background[38] with $B = 3006$ eV^2 and $C = 1643$ eV^2 parameters and after correction from analyser transmission function and photoionization cross sections[39] (see supplementary information of Ref. 25). To quantify thin Cr films, the second plasmon satellite of O 1s was subtracted from the Cr 2p line (see Fig. S1 of ESI†). Although the growth of Cr is not two-dimensional, Cr thickness was estimated through a model of signal damping in a thin continuous film[40] using effective attenuation lengths (supplementary information of Ref. 25), bulk density and stoichiometry of Cr or Cr_2O_3. Low-energy electron diffraction (LEED) patterns of chromium deposits on alumina suffer from charge effects and from the lack of any diffraction spots. Those effects are likely related to the growth of a non-epitaxial layer and/or to nanoparticles[25]. To circumvent the problem, the crystallography of the Cr/alumina film was analyzed by reflection high energy electron diffraction (RHEED).

X-ray Absorption Spectroscopy (XAS) measurements were performed on the LUCIA beamline at synchrotron SOLEIL (France) in a UHV apparatus that involves the preparation and main chambers (2.10^{-10} mbar)[41]. Near-edge (XANES) and extended (EXAFS) spectra were collected at the Cr K edge (around 6000 eV) in total electron yield mode by using a Si(111) monochromator. XAS spectra for the pure Cr metal and Cr_2O_3 oxide were collected as reference compounds. Data analyses were done using ATHENA and ARTEMIS packages[42]. Due to diffraction peaks from the alumina substrate, the extent of the EXAFS data is limited to 8 Å^{-1} while the R-domain spans from 0.5 to 3 Å. Phase functions were extracted from FEFF9 calculations[43] on Cr_2O_3 (Cr-O pairs), Cr metal (Cr-Cr pairs) and the intermetallic compound Cr_5Al_8 for Cr-Al pairs.

Once introduced in vacuum in either apparatus, one-side epipolished $(9 \times 9 \times 0.5)$ mm^3 α-Al_2O_3 (0001) single crystals (supplier MaTecK[44]) were annealed at $\sim 1200 - 1500$ K by electron bombardment of the holder under oxygen provided by a doser put at a millimetre distance of the surface to increase by more than one order of magnitude the local oxygen pressure[45] (stationary pressure 2.10^{-6} mbar). Such a preparation led to a sharp (1×1) LEED pattern. Contaminants, in particular carbon, were below the detection limit of XPS, except for calcium which segregates from bulk up to a maximum apparent coverage of 1 Å. Since such segregated Ca does not impact the long-range surface crystalline structure of alumina[46–48], is absent from the local environment of Cr probed by XAS[24] and does not evolve upon Cr deposition (*i.e.* the Ca 2p level is unaffected), its presence was assumed not to affect the chemical state of Cr. Cr was evaporated on substrates at room temperature from a metallic rod heated by electron bombardment (Omicron EFM3) whose flux was calibrated by a quartz microbalance (rate ~ 1 Å.s^{-1}). However, thicknesses used herein refer only to XPS and XAS determination. This latter is achieved through a comparison of absorption threshold jumps. Although no significant metallic Cr ageing was observed over the time scale of measurements in either set-up, new substrates were systematically used for each deposit. As a reference, a Cr oxide film (thickness 16.2 Å), hereafter labelled reference Cr oxide, was obtained by a prolonged oxidation at $T \sim 1575$ K of a thick Cr film under gas doser ($p = 2.10^{-6}$ mbar).

2.2 Computational details

All calculations were performed within the framework of the density functional theory (DFT) using the plane wave projector augmented-wave[49] (PAW) method implemented in the Vienna Ab-initio Simulation Package (VASP)[50–53]. Exchange-correlation effects were treated with dispersion-corrected optB88-vdW functional[54,55]. Moreover, DFT+U approach proposed by Dudarev[56,57] was applied to all configurations which involved Cr ions ($U_{Cr} = 3$ eV). Indeed, a solely vdW-DFT estimation may lead to an non-negligible (about 1 eV) underestimation of Cr 2p core level shifts (CLS) in configurations where Cr is ionized. The basis set included plane waves up to a kinetic energy of 400 eV.

As to describe Cr adatoms in a variety of realistic environments, alumina surface with Cr+O_3, Cr+O_2, Cr+O_2H, and Cr+O adspecies, which have been identified as thermodynamically stable under H-lean conditions[24] have been considered. These configurations involve Cr in +6, +4, +3, and +2 formal oxidation states, respectively. As a reference, an isolated Cr adatom on the alumina surface was also considered. All these configurations were modelled with a single Cr adatom [per (1 × 1) unit cell] adsorbed in the favoured hollow site of the Al-terminated Al_2O_3(0001) surface[24]. The alumina substrate was represented by a slab composed of seven Al_2O_3 layers at the experimental in-plane bulk lattice parameter of 4.785 Å. The adspecies were adsorbed symmetrically on both slab surfaces and the coordinates of all atoms were relaxed until forces got lower than 0.01 eV$Å^{-1}$. Furthermore, as to make a direct link to metallic Cr in bulk chromium and to Cr cations in bulk chromia, the same alumina slabs were sandwiched with five monolayer thick slabs of either metallic chromium or Cr_2O_3. In these superstructure calculations also the length of lattice vector perpendicular to the interfaces was optimized. Finally, reference bare Al-terminated and OH-covered Al_2O_3(0001) surfaces were also considered for CLS calculations. In all the ground state calculations, the Brillouin zone of the (1 × 1) surface cell was sampled with a Γ-centered (8 × 8) Monkhorst-Pack mesh.

The CLSs were further calculated in the complete screening approach[58,59], which includes the response of the valence electrons to the creation of a core hole. Screening by the other core-electrons was not taken into account, as it is generally environment-independent and therefore does not significantly influence the CLS[58]. The ground state configurations in a (3 × 3) surface unit cell were used as to minimize the interaction between the excited ions. Restricting the Brillouin-zone sampling to the Γ point turned out to be sufficient.

3 Chemistry and structure of Cr/alumina

3.1 Cr chemical state evolution from photoemission and XAS

Fig. 1-a displays a series of Cr 2p spectra recorded for selected Cr/α-Al_2O_3(0001) films, either metallic or purposely oxidized. The corresponding Cr $2p_{3/2}$ core level shift are given in Fig. 1-b as a function of the Cr thickness as well as that of the reference Cr oxide. They are compared to tabulated CLS related to Cr([Ar]$3d^5 4s^1$) formal oxidation states, from Cr^0 to Cr^{6+}, among which the most common and stable is Cr^{3+} (average values from database Ref. 37): 574.2 ± 0.25 eV (Cr metal, Cr^0), 577.2 ± 0.2 eV ($Cr(OH)_3$, Cr^{3+}), 576.6 ± 0.6 eV (Cr_2O_3, Cr^{3+}), 575.85 ± 0.6 eV (CrO_2, Cr^{4+}), 579.3 ± 0.6 eV (CrO_3, Cr^{6+}). The tabulated apparent spin orbit splitting of the Cr 2p doublet is 9.25 ± 0.08 eV for Cr metal (Cr^0), 9.72 ± 0.2 eV for Cr_2O_3 eV (Cr^{3+}), 9.6 ± 0.14 eV for CrO_2 (Cr^{4+}).

Occurring in supported clusters[25], the Cr $2p_{3/2}$ shifts could involve a final state screening of the positive photo-hole[60–63]; an estimate is given by $E_{F,m} = \alpha e^2/4\pi\varepsilon_0 R$, where R is the particle radius, ε_0 the vacuum permittivity and α a parameter around 0.5[61,62], so that the observed shift of ~ 1 eV could stem from clusters of around 1.5 nm in size. However, several arguments favour chemistry instead of electrostatics. Firstly, the Cr 2p line clearly exhibits a shoulder at higher binding energy, the overall contribution of which decays as the growth proceeds (Fig. 1-a). Other arguments come from XAS analysis. Fig. 2 compares Cr K-edge XAS spectra and modulus of corresponding Fourier transforms (FT) of various deposits and substrates: (a) 1.0 Å thick Cr film and bulk Cr_2O_3; (b) 1.5 and 2.5 Å thick Cr films; (c) 15 Å thick Cr film and bulk Cr metal. Very similar contributions attributed to oxidized Cr are observed, in both edge and FT modulus, on the 1.0 Å, 1.5 Å and 2.5 Å thick films (Fig. 2-a,b), which were shown to match distances and environments found in Cr-O_2H moieties[24]. The 15 Å thick Cr film[24] compares to bulk metal (Fig. 2-c) although a small contribution is observed for similar Cr-O distances observed with thinner coverages. Therefore, XAS demonstrates the occurrence of a defined interfacial oxidized environment in all Cr films.

To clarify the change of Cr chemistry and environment, the Cr 2p line shape evolution was quantitatively analysed by focussing firstly on reference spectra of Cr metal and oxide (Fig. 3). Fits[64] were performed with Doniach-Sunjic[65] and Voigt profiles accounting for the X-ray source satellites[66] with a fixed 1/2 theoretical branching ratio of the 2p lines and for an active Tougaard background[38]. The Lorentzian broadening was fixed at the X-ray source width (0.58 eV for Al-Kα and 0.54 for Mg-Kα) while the variable Gaussian width described instrumental resolution and distribution of chemical environments. The Cr 2p line shape recorded on the 17.7 Å thick metallic film involves a Doniach-Sunjic profile (asymmetry $\alpha = 0.35$) and a plasmon shifted by 24 eV[67]; the interface contribution in this case remains negligible. The Cr 2p profile of the reference Cr oxide was fitted with a main line and a shake-up satellite shifted by 11.8 eV (Fig. 3-b), as in the case of Cr_2O_3[68–73]; the complex multiplet splitting of the main line[68–76] is accounted for in an effective way by an asymmetric line shape. Spin-orbit splitting (9.2 for the metal and 9.8 eV for the oxide) and asymmetric line shapes match with expectations of Cr^0 and Cr^{3+}[37]. Above all, the E_B(Cr $2p_{3/2}$) of 574.0 eV and 576.2 ± 0.25 eV recorded on the metal and oxide, respectively, fairly agrees with tabulated values (574.2 ± 0.25 eV for Cr metal and 576.6 ± 0.6 eV for Cr_2O_3[37]). These two measurements increase our confidence in the employed binding energy scale calibration. In the XPS analysis of Cr/alumina, the overlap between O KLL and Cr LMM Auger transitions prevents the determination of Cr chemistry via Auger parameter, which led to use the tabulated Al 2s peak position

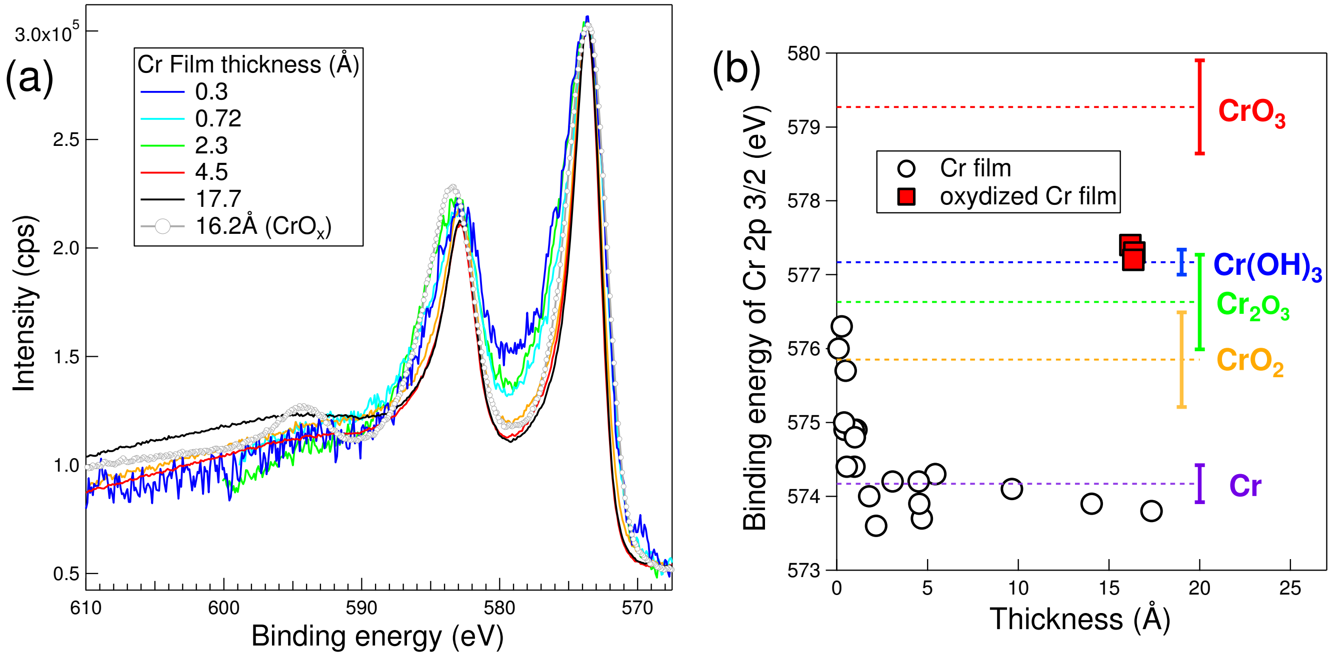

Fig. 1 Cr 2p core levels from Cr/Al_2O_3(0001) films: (a) photoemission spectra aligned on background and peak maximum to highlight line shape changes. Bare surface spectra have been subtracted after suitable intensity normalization to remove the double plasmon excitation of O 1s below Cr $2p_{1/2}$. A comparison is made with a thick purposely oxidized Cr film (CrO_x). Charge effects have been corrected by using Al 2s binding energy as an internal reference. (b) Evolution of the Cr $2p_{3/2}$ binding energy with Cr thickness (circles). Squares correspond to the oxidized Cr film. For comparison, average (horizontal lines) and range (error bars) of tabulated values are given for various Cr oxidation states on corresponding bulk (hydr)oxides[37] (see text).

($E_B = 119.6$ eV[37]) as a reference to overcome charge effects. Constant Al 2s profile (see below) and E_B(O 1s) $= 531.5 \pm 0.1$ eV value justify the approach.

Even at very low Cr/alumina coverage, visual inspection of Cr $2p_{3/2}$ profiles (Fig. 1-a) and fits indicate that Cr films involve both metal and oxide. To enhance the relative contribution of the oxide, an example of Cr/alumina film was taken in the submonolayer Cr coverage range (0.34 Å); the corresponding Cr 2p, O 1s and Al 2s core levels are shown in Fig. 4. After substraction of the second order of the O 1s plasmon satellite at low thicknesses (Fig. S1 of ESI†), the Cr 2p profile was decomposed into two components corresponding to metallic and oxidized Cr (Fig. 4-a). The above defined line shape (Fig. 3-a) and energy position (E_B(Cr $2p_{3/2}$)=574.0 eV) were used to represent the metallic contribution of the Cr 2p spectra. A spin-orbit splitting of 9.7 eV and a Cr 2p CLS of +2.5 eV were found to accurately represent the oxide component. However, the complex multiplet splitting and shake-up satellite were ignored. Such a pragmatic fitting approach[69,70,72,73] yielded to an oxidized component broader ($\mathrm{FWHM}_G \simeq 5.2$ eV) than the metallic one ($\mathrm{FWHM}_G \simeq 2.2$ eV). The equivalent thickness of oxidized metal was estimated to 0.07 ± 0.02 Å in the (110) body-centred stacking of Cr with a lattice parameter of 2.91 Å. Assuming a Cr+O_2H adsorption configuration[24], such an amount corresponds to a reaction with 1.1 ± 0.3 OH.nm^{-2}. At higher Cr coverage, Cr 2p spectra can be fitted in a similar way (Fig. S2 of ESI†) but, because of the decrease in the relative weight of the component which corresponds to the oxide, the quantitative analysis becomes less reliable. However, a key point is that the oxide contribution keeps a constant profile and decreases in relative intensity (Fig. S2 of ESI†), which supports the XAS view of the absence of formation of intermediate oxidation states at the Cr/Cr-O_2H interface.

3.2 Crystallinity of metallic Cr/alumina films

The status of metallic Cr remains unclear since metallic environment with Cr-Cr distances of 2.50 and 2.91 Å characteristic of body-centred cubic structure is only observed in thicker Cr films (here 15 Å), although the previously obtained number of Cr neighbours does not match that found in bulk metal[24]. In Table 1 of Ref. 24, the fitting procedure set-up was kept identical to that used for thin films. This led to abnormally low coordination numbers for the thick Cr film. For a more precise description of this thick film, the initial parameters were allowed to go towards those of Cr metal. This did not change the oxygen coordination, but increased the Cr-Cr coordination numbers and the disorder parameters to values in line with an ill-crystallized metallic layer built on top of a first layer of Cr-O moieties, analogous to those found in the very thin film. In agreement, the near edge structure of the 15 Å Cr film is closer to bulk Cr metal than to Cr oxide (Fig. 2-c). In particular the pre-edge at 5995 eV is characteristic of 3d-metals. The decrease in intensity of the main FT peak at 1.35 Å (associated to Cr-O) as the Cr thickness increases (Fig. 2-a,b) can be related to a growing proportion of Cr atoms not directly linked to oxygen. Nevertheless the

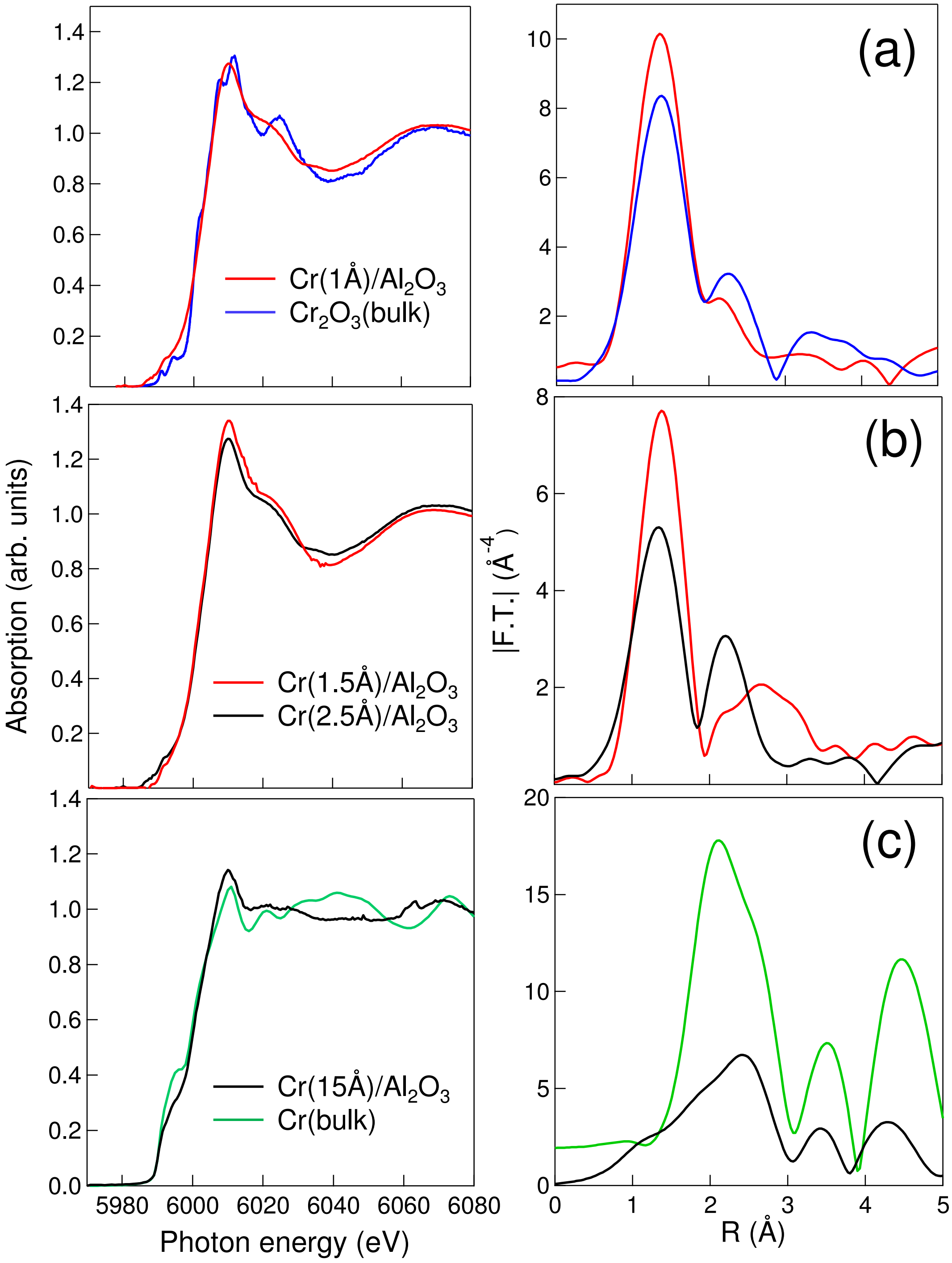

Fig. 2 XAS spectra (left) and modulus of the extended x-ray absorption fine structure (EXAFS) Fourier transform (right) at the Cr K edge for the following samples: (a) 1.0 Å thick Cr/alumina film (red) and bulk Cr_2O_3 (blue); (b) 1.5 (red) and 2.5 Å (black) thick Cr/alumina films; (c) 15 Å thick Cr/alumina film (black) and bulk Cr metal (green).

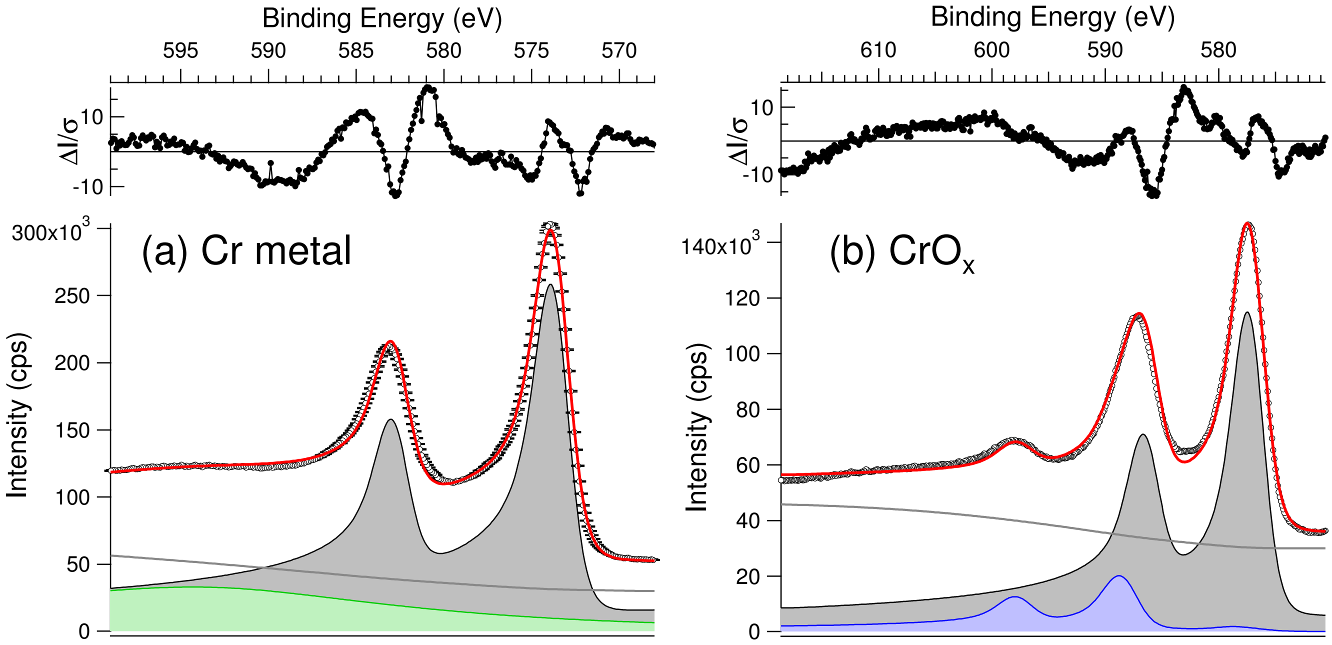

Fig. 3 Fit (red line) of the Cr 2p core level (black points) in Cr/alumina films (see text): (a) 17.7 Å thick Cr film; the metallic component (grey) of Doniach-Sunjic line shape is accompanied by a broad plasmon (green); (b) purposely oxidized 16.2 Å thick Cr film; both the main line shape (grey) and the shake-up satellite (blue) are featured. In both figures, the grey lines correspond to the Tougaard background and the top line to residuals normalized by error taken as the square-root of the intensity.

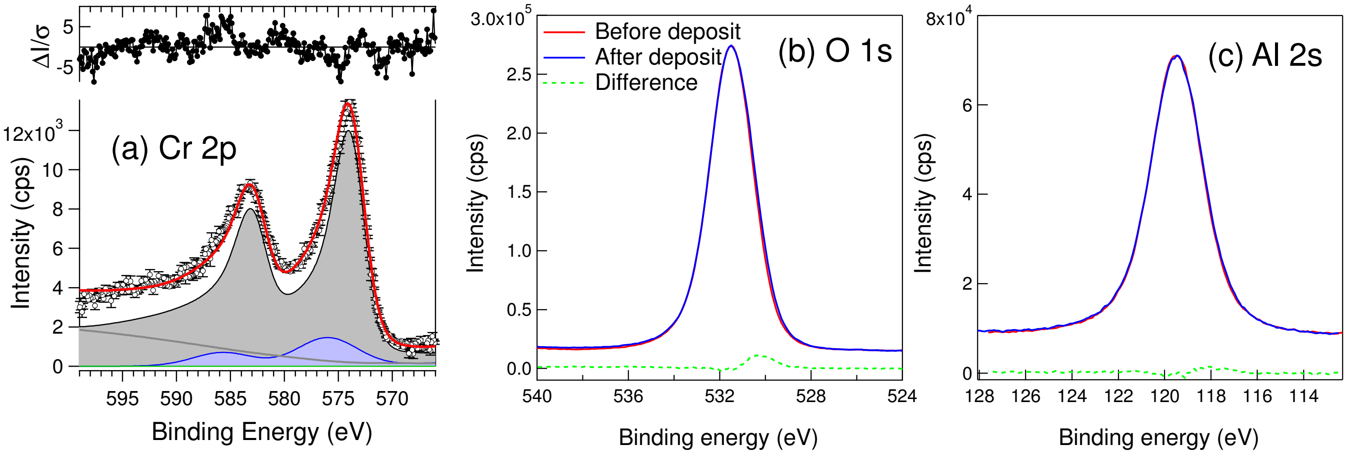

Fig. 4 Core level profiles of a Cr(0.34 Å)/alumina deposit: (a) Fit (red line) of the Cr 2p core level (black points) with metallic (grey curve) and oxidized (blue curve) components (see text for explanations), (b) O 1s and (c) Al 2s. The difference curve before and after deposition is shown as a dotted line in Figs.-b,c.

near edge structure of intermediate thicknesses remains very similar to that of the thinner deposit, without combined Cr-Cr distances around 2.5 and 2.90 Å, which are the signature of metallic Cr. The second FT peak is difficult to model properly in these films, but it is made of an increasing number of disordered Cr-Cr distances between 2.5 and 2.9 Å. The link between the two structures could be the Cr-Cr distance at 2.9 Å which is common to Cr_2O_3 and Cr metal.

The poor crystallinity of the Cr film, which perturbs the fitting process of the EXAFS data, is supported by RHEED analysis. Fig. 5-a shows a set of diffraction patterns recorded at different Cr thicknesses for an electron beam aligned along the [100] direction of $Al_2O_3(0001)$. As seen directly from the pattern (Fig. 5-a), the intensity profiles (Fig. 5-b) or the integrated intensity compared to background (Fig. 5-c), diffraction rods of the alumina surface rapidly vanish to reach a nearly uniform background level beyond a Cr thickness of about 5 Å. Only for thick Cr films, a low contrast ring shape typical for a poorly crystallized or amorphous layer is recovered (pink line in Fig. 5-a). This ring is isotropic as it is independent of the sample azimuth. The comparison of its radius to the reference on the bare alumina gives a distance of $d = 2.57 \pm 0.05$ Å in line with metallic Cr. This lack of crystallinity of the Cr films, as seen by RHEED, agrees with the absence of definite local order for Cr not linked to oxygen which is inferred from XAS analysis.

4 Core level shifts determined by *ab initio* calculations to understand the Cr/alumina interface

Chemicals shifts of all elements involved in the Cr/alumina system are now analysed as a whole. In parallel to Cr deposition, slight changes in O 1s (Fig. 4-b) and Al 2s (Fig. 4-c) profiles are observed, with contributions shifted by -1.3 ± 0.3 eV (O 1s) and ~ -1.1 to -2 eV (Al 2s). These are now compared to calculated counterparts (Fig. 6). Numerical simulations representing all degrees of Cr oxidation have been performed by a DFT+U approach ($U = 3$ eV) on purposely designed configurations CrO_x (Table 1) corresponding to a Cr coverage of the order of a monolayer, as in experiments, since comparison with values recorded on bulk compounds (Fig. 1-b) are not fully relevant in such a context. Selected structures involve Cr^{6+}, Cr^{4+}, Cr^{3+}, and Cr^{2+} oxidation states, which were shown to be thermodynamically the most stable among configurations formed upon reaction of Cr with surface OH groups on alumina[24]. The isolated Cr adatom (Cr^0), Cr in the oxide Cr_2O_3 and in bulk Cr metal ($U = 0$ eV) have also been calculated, as well as bare and water-covered $Al_2O_3(0001)$ surfaces that are taken as references for O 1s and Al 2s core levels. All these atomic configurations are displayed on the periphery of Fig. 6.

Fig. 6 is a guide for the discussion that follows, with appropriate color codes for the debated configurations, CLS and atoms. The present and tabulated[37] absolute E_B(Cr 2p) values related to Cr metal and Cr_2O_3, and the corresponding theoretical CLS nicely compare (Fig. 6-a,b). The value of the O 1s CLS associated to surface OH recorded at 1.4-1.5 eV from the bulk component (Fig. S3 of ESI†), in agreement with the commonly found values of 1.3-1.6 eV[18,77–79] agrees in trend with the present theoretical estimate (2.3 eV, Fig. 6-b). Indeed, the calculated absence of O 1s shift of terminal O atoms associated to the bare α-$Al_2O_3(0001)$ (Fig. 6-b) discards the interpretation[80] of the 1.3-1.6 eV shift observed after annealing in vacuum as related to the bare surface and argues for the assignment of that shift to surface OH. This point is important as OH groups strongly impact the wetting of alumina surface by metals [22,24,78,79,81] and, more speculatively, the dispersion of its isoelectric point[82] and its structure[83]. Clearly, the poorly understood residual OH coverage is a key to the surface properties of the oxide. The correct agreement between measurements and calculations for those well-defined systems (Cr metal and oxide, surface OH of alumina) proves the robustness of the calculations which include final state effects and validates the employed U value.

The experimental value of 2.5 eV for the Cr 2p shift associated to the oxidized Cr in Cr/alumina films is very discriminating. It reasonably agrees with CLS values calculated for Cr^{3+} (Cr-O_2H) and Cr^{4+}, but it much differs from what is expected for Cr^{6+}, Cr^{2+} and Cr^0 (Fig. 6-a). CLS related to O 1s support the finding although they are less discriminating (Fig. 6-b). However, there is a clear gap between the O 1s shift associated to Cr_2O_3 and that related to the oxide component of the Cr/alumina (Fig. 6-b), which confirms that the latter species differs from the bulk oxide. In addition, the only calculated Cr-O distances that match the XAS analysis are those found in the Cr-O_2H moieties[24] (Table 1). The Al 2s profile changes upon Cr deposition, with a contribution shifted by ~ -1.1 to -2 eV with respect to the bulk component (Fig. 4-c). Such an Al 2s shift is much smaller than that which is expected between the Al metal and Al_2O_3 (-2.7 to -3.3 eV)[18,37]. In agreement with the picture derived by optics[25] of metallic Cr clusters anchored by oxidized entities that cover progressively the surface and the limited fraction of oxidized Cr as shown by the Cr 2p profile (Fig. 1 and Fig. S2 of ESI†), the experimental Al 2s CLS matches that characteristic of a contact between bulk Cr and alumina (Fig. 4-c). Therefore, the reduction of the α-$Al_2O_3(0001)$ substrate by Cr[33,34] is ruled out, in agreement with the DFT approach[24] and in a manner similar to Ti[18,84] or Co[79], which confirms that the reaction with surface OH groups[24] is the only route for Cr oxidation. However, contrary to what was observed for Ti/alumina[18], no depletion due to the reaction of Cr with OH[24] appears on the higher O 1s binding energy side (Fig. 4-b). This leads to postulate a compensation of the depletion by inelastic energy losses undergone by photoelectrons on their way through the Cr metallic film, as evidenced at the Ti/alumina interface[18]. The argument is supported by the systematic presence of metallic Cr in Cr 2p core level even for the lowest deposited Cr amount (Fig. 4-a).

Overall, the XPS analysis shows that, upon Cr deposition, the Cr film involves an oxidized Cr species in limited amount and

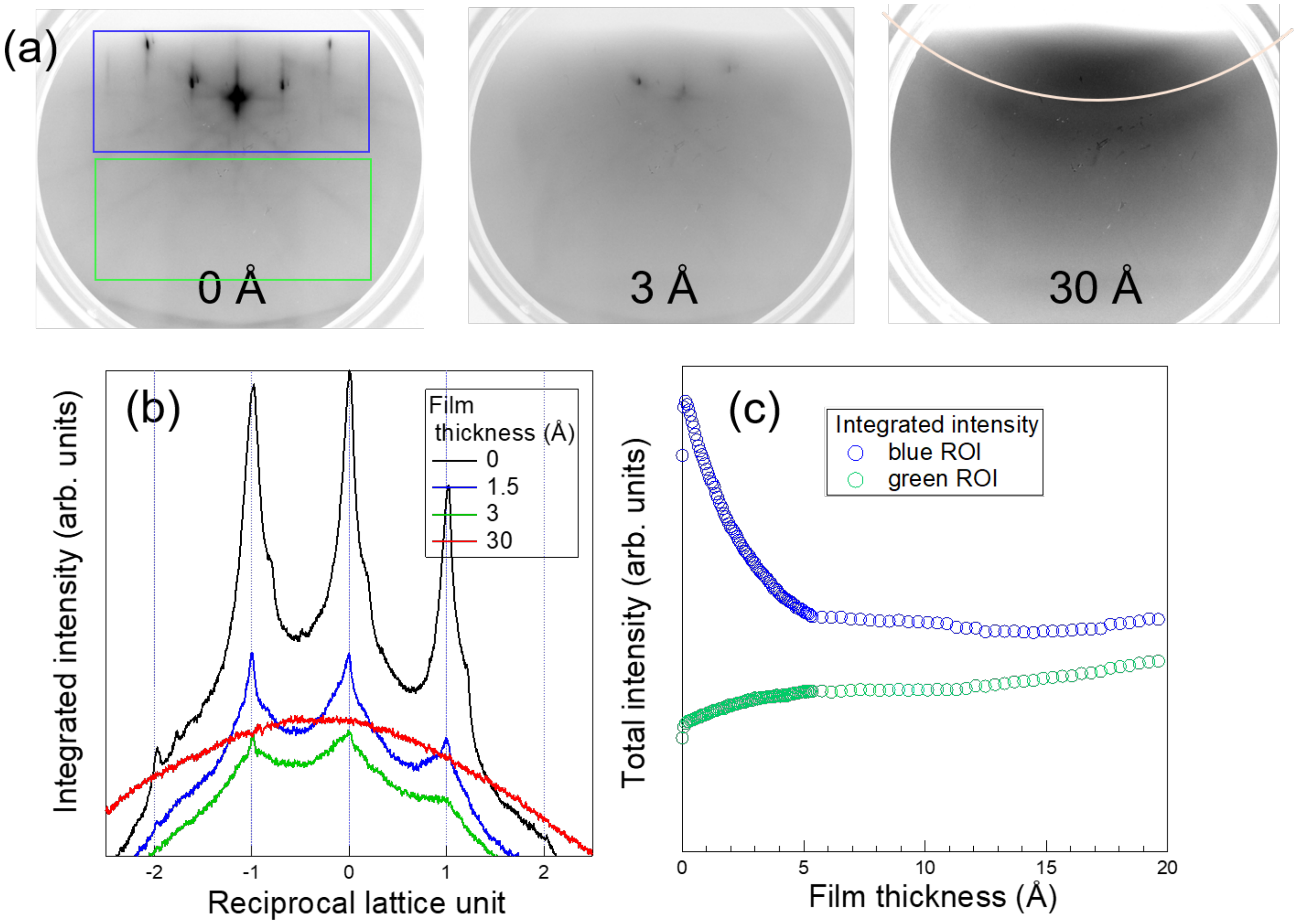

Fig. 5 (a) Evolution of the RHEED diffraction pattern (beam energy of 9.5 keV) along the [100] direction of Al_2O_3(0001) upon Cr deposition. Film thickness calibrated by XPS is given on the figure. The pink line at the end of the deposit points to a polycrystalline layer; (b) Intensity cross section (integrated over the blue region of interest (ROI) of figure-a) as a function of alumina reciprocal space coordinate; (c) Integrated signal (blue ROI) and background (green ROI) of figure-a versus film thickness. The evaporation rate was ~ 0.4 Å/min.

config.	Q_{Cr}	μ_{Cr}	Cr^{z+}	$d(Cr-O)$
Cr+O_3	+2.1	0.0	6	2.13, 2.13, 2.13; 1.66, 1.66, 1.66
Cr+O_2	+1.8	2.1	4	1.95, 2.17, 2.19; 1.70, 1.71
Cr+O_2H	+1.6	2.9	3	1.98, 2.04, 2.18; 1.79, 1.89
Cr+O	+1.3	3.9	2	2.09, 2.33, 2.38; 1.96
Cr	+0.8	4.3	0	2.32, 2.28, 2.08
Cr_2O_3	+1.7	2.8	3	2.02, 2.02, 2.02, 1.95, 1.95, 1.95
Cr (metal)	+0.0	0.4	0	

Table 1 Calculated electronic and structural characteristics of Cr atoms in the different considered configurations: Bader charges Q_{Cr} (e), magnetic moments μ_{Cr} (μ_B), formal oxidation states Cr^{z+}, and Cr-O bond lengths $d(Cr-O)$(Å). For adspecies, the first three bond lengths correspond to these with oxygen atoms in the Al_2O_3 substrate.

metallic Cr that coexist from the very beginning of the formation of the interface. Despite the limits of the present comparisons, in which theory approximates complex situations with model structures[24], reasonable agreements are found. The oxide stems from the reaction of Cr with surface OH, the reduction of the substrate by Cr being totally excluded. The Cr 2p, O 1s and Al 2s CLS observed upon Cr deposition are compatible with the formation of the previously identified Cr-O_2H moieties, although photoemission alone does not discriminate between Cr^{3+} and Cr^{4+} oxidation states. Metallic Cr clusters grow partly in contact with the alumina substrate, *i.e* independently of the Cr oxide, although Cr-O distances characteristic of the Cr/alumina interface are not evidenced in XAS. Such a configuration is in full agreement with the model of seed layer which was previously derived from optical measurements[25].

5 Conclusion

Chemical states of all the elements involved in the Cr/α-Al_2O_3(0001) interface have been analysed by photoemission and x-ray absorption spectroscopy combined with the determination of chemical shifts by density functional approach involving final state effects. This scarcely-employed combination of spectroscopic measurements and calculations demonstrates that, at the onset of its deposition, Cr is oxidized by reaction with the surface OH groups to mainly form Cr^{3+} in the form of Cr+O_2H moieties, in agreement with previous findings[24], although the formation of Cr^{4+} is not excluded. Cr does not reduced the alumina substrate. Most importantly, some Cr is initially deposited in metallic form, in parallel to oxidized species, but the formation of intermediate oxidation states at the Cr/Cr-O_2H interface is excluded, which fully supports the previously described Cr/alumina buffer mechanism[25]. A difficulty in analysing the (Cr+Cr oxide)/alumina interface arises from the poorly ordered character of Cr, at long and even at short distances, up to large thicknesses. This situation is likely caused by the presence of oxidized Cr at the interface although the well-known low-diffusivity of Cr may also impact the ordering[25]. The study of chemical states (photoemission and near-edge spectroscopy) then become a pivotal approach of the system.

Conflicts of interest

There are no conflicts to declare.

Acknowledgements

The team in charge of the SOLEIL machine is warmly acknowledged as well as D. Roy (LUCIA) for his technical assistance. This work was supported by French state funds managed by the ANR within the Investissements d'Avenir program under reference ANR-11-IDEX-0004-02, and more specifically within the framework of the Cluster of Excellence MATISSE led by Sorbonne Universités.

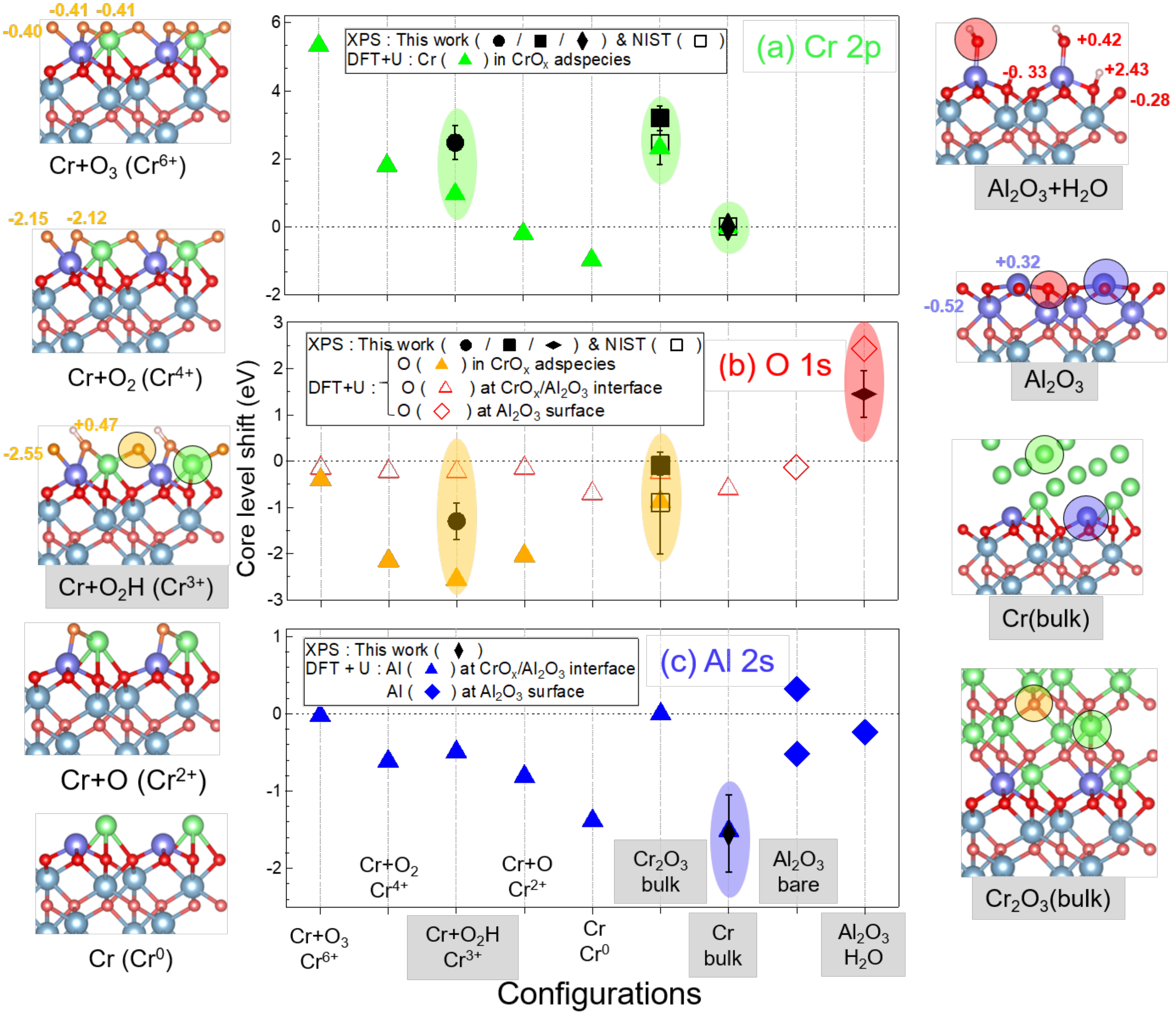

Fig. 6 Comparison between experimental (this work : black filled symbols; NIST references : black opened squares) and calculated (triangles and diamonds) core level shifts: (a) Cr 2p, (b) O 1s and (c) Al 2s. Calculations are done by DFT+U ($U_{Cr} = 3$ eV) for the configurations which are represented as ball models on each side of the figure (bulk Al: light blue; Al_2O_3 surface Al: blue; bulk O : light red; Al_2O_3 surface O: red; O in Cr+O_x adspecies: orange; H : white). Adsorbed Cr/alumina configurations with their formal oxidation states appear on the left hand side: Cr^{6+} (Cr+O_3), Cr^{4+} (Cr+O_2), Cr^{3+} (Cr+O_2H, Ref. 24), Cr^{2+} (Cr+O), Cr^0 (Cr). Atomic configurations related to bulk compounds (Cr^{3+} (Cr_2O_3) and Cr bulk metal) and alumina surface (bare Al_2O_3 and hydroxylated Al_2O_3+H_2O) appear on the right hand side. Theoretical CLSs are referenced to atoms in the center of the bulk Cr slab (Fig. a, Cr 2p, green triangles) and to atoms in the center of the Al_2O_3 slab (Fig. b, O 1s, yellow triangles; Al 2s, Fig. c, blue triangles). O 1s CLS at the Cr+O_x/Al_2O_3 are shown in Fig. b as red empty triangles. Similar convention was adopted for Al_2O_3 and Al_2O_3+H_2O (Fig. b: red empty diamonds; Fig. c: blue filled diamonds). Extra-values of CLSs are given on an atom-by-atom basis in the ball models. The configurations whose calculated chemical shifts are compared to the experiment are highlighted by shaded grey areas. In Fig. a, b and c, comparisons are indicated by light green (Cr 2p), yellow (O 1s in Cr+O_x), red (O 1s at Cr+O_x/Al_2O_3 interfaces) and blue (Al 2s) areas. In configurations drawn on each side of the figure, corresponding atoms are indicated by circles of the same colors.

Notes and references

1 K. Fukuda, S. H. M. Lim and A. Anders, *Thin Solid Films*, 2008, **516**, 4546–4552.

2 H. Aouani, J. Wenger, D. Gérard, H. Rigneault, E. Devaux, T. W. Ebbesen, F. Mahdavi, T. Xu and S. Blair, *ACS Nano*, 2009, **3**, 2043–2048.

3 V. J. Logeeswaran, N. P. Kobayashi, M. S. Islam, W. Wu, P. Chaturvedi, N. X. Fang, S. Y. Wang and R. S. Williams, *Nano Letters*, 2009, **9**, 178–182.

4 T. Siegfried, Y. Ekinci, O. J. F. Martin and H. Sigg, *ACS Nano*, 2013, **7**, 2751–2757.

5 M. Todeschini, A. Bastos da Silva Fanta, F. Jensen, J. B. Wagner and A. Han, *ACS Applied Material & Interfaces*, 2017, **9**, 37374–37385.

6 N. Formica, D. S. Ghosh, A. Carrilero, T. L. Chen, R. E. Simpson and V. Pruneri, *ACS Applied Materials & Interfaces*, 2013, **5**, 3048–3053.

7 R. Henriquez, R. Roco, S. Bravo, V. Del Campo, C. Gonzalez-Fuentes, S. Donoso and P. Häberle, *Appl. Surf. Sci.*, 2019, **489**, 403–408.

8 G. Dehm, C. Scheu, M. Rühle and R. Raj, *Acta. Mater.*, 1998, **46**, 759–771.

9 M. Sterrer and H. J. Freund, *Catal. Lett.*, 2013, **143**, 375–385.

10 S. L. Hemmingson and C. T. Campbell, *ACS Nano*, 2017, **11**, 1196–1203.

11 C. T. Campbell, S. C. Parker and D. E. Starr, *Science*, 2002, **298**, 811.

12 Q. Fu and T. Wagner, *Surf. Sci. Rep.*, 2007, **62**, 431–498.

13 A. G. Evans, J. W. Hutchinson and Y. Wei, *Acta Mater.*, 1999, **47**, 4093–4113.

14 C. V. Thompson, *Annu. Rev. Mater. Res.*, 2012, **42**, 399–434.

15 P. Jacquet, R. Podor, J. Ravaux, J. Teisseire, I. Gozhyk, J. Jupille and R. Lazzari, *Scr. Mater.*, 2016, **115**, 128 – 132.

16 P. Jacquet, R. Podor, J. Ravaux, J. Lautru, J. Teisseire, I. Gozhyk, J. Jupille and R. Lazzari, *Acta Mater.*, 2018, **143**, 281 – 290.

17 H. Liu, B. Wang, E. S. P. Leong, P. Yang, Y. Zong, G. Si, J. Teng and S. A. Maier, *ACS Nano*, 2010, **4**, 3139–3146.

18 R. Lazzari and J. Jupille, *Phys. Rev. B*, 2005, **71**, 045409.

19 G. Kästle, H. G. Boyen, B. Koslowski, A. Plettl, F. Weigl and P. Ziemann, *Surf. Sci.*, 2002, **498**, 168–174.

20 R. Cavallotti, H.-L. Thi Le, J. Goniakowski, R. Lazzari, J. Jupille, A. Koltsov and D. Loison, *Phys. Chem. Chem. Phys.*, 2016, **18**, 3032–3039.

21 H.-A. T. Le, J. Goniakowski, C. Noguera, A. Koltsov and J.-M. Mataigne, *J. Phys. Chem. C*, 2016, **120**, 9836–9844.

22 H.-L. Thi Le, R. Lazzari, J. Goniakowski, R. Cavallotti, S. Chenot, C. Noguera, J. Jupille, A. Koltsov and J.-M. Mataigne, *J. Phys. Chem. C*, 2017, **121**, 11464–11471.

23 H.-L. T. Le, J. Goniakowski, C. Noguera, A. Koltsov and J.-M. Mataigne, *J. Phys. Chem. C*, 2017, **121**, 25143–25151.

24 M. Messaykeh, J. Goniakowski, G. Cabailh, J. Jupille, R. Lazzari, P. Lagarde and N. Trcera, *J. Phys. Chem. C*, 2019, **123**, 29245–29254.

25 M. Messaykeh, S. Chenot, P. David, G. Cabailh, J. Jupille, A. Koltsov and R. Lazzari, *Crystal Growth & Design*, 2021, **21**, 3528–3539.

26 M. Guttmann, Reactive phase formation at interfaces and diffusion processes, 1994, pp. 527–548.

27 P. Drillet, Z. Zermout, D. Bouleau, J. Mataigne and S. Claessens, *La Revue de Métallurgie-CIT*, 2004, **101**, 831–837.

28 Z. Dai, P. Borghetti, S. Chenot, P. David, J. Jupille, G. Cabailh, J. Goniakowski and R. Lazzari, *Appl. Surf. Sci.*, 2019, **492**, 886–895.

29 Z. Dai, N. Alyabyeva, P. Borghetti, S. Chenot, P. David, A. Koltsov, G. Renaud, J. Jupille, G. Cabailh and R. Lazzari, *Appl. Surf. Sci.*, 2020, **509**, 145312.

30 Z. Dai, N. Alyabyeva, M. Van den Bossche, P. Borghetti, S. Chenot, P. David, A. Koltsov, G. Renaud, J. Jupille, G. Cabailh, C. Noguera, J. Goniakowski and R. Lazzari, *Phys. Rev. Materials*, 2020, **4**, 074409.

31 E. Søndergård, O. Kerjan, D. Abriou and J. Jupille, *Eur. Phys. J. D*, 2003, **24**, 343–345.

32 M. Yoshitake, S. Yagyu and T. Chikyow, *J. Vac. Sci. Technol., A*, 2014, **32**, 021102.

33 B. Ealet, B. Robrieux and E. Gillet, *J. Adhes. Sci. Technol.*, 1992, **6**, 1221–1231.

34 H. Lu, D. H. Shen, C. L. Bao and Y. X. Wang, *Physica Status Solidi (a)*, 1997, **159**, 425–437.

35 M. Eriksson, J. Sainio and J. Lahtinen, *J. Chem. Phys.*, 2002, **116**, 3870–3874.

36 J. Sainio, M. Eriksson and J. Lahtinen, *Surf. Sci.*, 2003, **532-535**, 396–401.

37 *NIST X-ray photoelectron spectroscopy database*, https://srdata.nist.gov/xps/Default.aspx.

38 S. Tougaard, *Surf. Interface Anal.*, 1997, **25**, 137–154.

39 J. Yeh and I. Lindau, *At. Data Nucl. Data Tables*, 1985, **32**, 1–155.

40 A. Jablonski, *Surf. Sci.*, 2019, **688**, 14–24.

41 R. Lazzari, J. Goniakowski, G. Cabailh, R. Cavallotti, N. Trcera, J. Jupille and P. Lagarde, *Nano Lett.*, 2016, **16**, 2574–2579.

42 B. Ravel and M. Newville, *J. Synchrotron Rad.*, 2005, **12**, 537–541.

43 http://feff.phys.washington.edu/feffproject-references.html.

44 http://www.physik.de/mateck.

45 C. T. Campbell and S. M. Valone, *J. Vac. Sci. Technol. A*, 1985, **3**, 408–411.

46 G. Renaud, B. Villette, I. Vilfan and A. Bourret, *Phys. Rev. Lett.*, 1994, **73**, 1825–1828.

47 P. Guénard, G. Renaud, A. Barbier and M. Gautier-Soyer, *Surf. Rev. Lett.*, 1998, **5**, 321.

48 G. Renaud, *Surf. Sci. Rep.*, 1998, **32**, 1–90.

49 P. E. Blöchl, *Phys. Rev. B*, 1994, **50**, 17953–17979.

50 G. Kresse and J. Hafner, *Phys. Rev. B*, 1994, **49**, 14251–14269.

51 G. Kresse and J. Furthmüller, *Phys. Rev. B*, 1996, **54**, 11169–

11186.

52 G. Kresse and J. Furthmüller, *Comp. Mater. Sci.*, 1996, **6**, 15–50.

53 G. Kresse and J. Joubert, *Phys. Rev. B*, 1999, **59**, 1758–1775.

54 J. Klimeš, D. R. Bowler and A. Michaelides, *J. Phys.: Condens. Matter*, 2010, **22**, 022201.

55 J. Klimes, D. R. Bowler and A. Michaelides, *Phys. Rev. B*, 2011, **83**, 195131.

56 V. I. Anisimov, F. Aryasetiawan and A. I. Liechtenstein, *J. Phys.: Condens. Matter*, 1997, **9**, 767–808.

57 S. L. Dudarev, G. A. Botton, S. Y. Savrasov, C. J. Humphreys and A. P. Sutton, *Phys. Rev. B*, 1998, **57**, 1505–1509.

58 L. Köhler and G. Kresse, *Phys. Rev. B*, 2004, **70**, 165405.

59 V. Nilsson, M. Van den Bossche, A. Hellman and H. Grönbeck, *Surf. Sci.*, 2015, **640**, 59–64.

60 G. K. Wertheim, S. B. DiCenzo and S. E. Youngquist, *Phys. Rev. Lett.*, 1983, **51**, 2310–2313.

61 H. Hövel, B. Grimm, M. Pollmann and B. Reihl, *Phys. Rev. Lett.*, 1998, **81**, 4608–4611.

62 A. Howard, D. N. S. Clark, C. E. J. Mitchell, R. G. Edell and V. R. Dhanak, *Surf. Sci.*, 2002, **518**, 210–224.

63 E. Chernysheva, W. Srour, B. Philippe, B. Baris, S. Chenot, R. F. Duarte, M. Gorgoi, H. Cruguel, H. Rensmo, H. Montigaud, J. Jupille, G. Cabailh, S. Grachev and R. Lazzari, *Phys. Rev. B*, 2018, **97**, 235430.

64 R. Lazzari, `Igor Pro Paris Photoemission Package` can be downloaded with a user guide from: http://www.insp.upmc.fr/I4P-Igor-Pro-Paris-Photoemission.html?lang=en.

65 S. Doniach and M. Sunjic, *Journal of Physics Part C : Solid State Physics*, 1970, **3**, 285–291.

66 C. Klauber, *Surf. Interface Anal.*, 1993, **20**, 703–715.

67 H. Kato, Y. Sakisaka, M. Nishijima and M. Onchi, *Surf. Sci.*, 1981, **107**, 20 – 30.

68 E. Ünveren, E. Kemnitz, S. Hutton, A. Lippitz and W. E. S. Unger, *Surf. Interface Anal.*, 2004, **36**, 92–95.

69 I. Grohmann, E. Kemnitz, A. Lippitz and W. E. S. Unger, *Surf. Interface Anal.*, 1995, **23**, 887–891.

70 A. M. Salvi, J. E. Castle, J. F. Watts and E. Desimoni, *Appl. Surf. Sci.*, 1995, **90**, 333 – 341.

71 A. R. Pratt and N. S. McIntyre, *Surf. Interface Anal.*, 1996, **24**, 529–530.

72 M. Aronniemi, J. Sainio and J. Lahtinen, *Surf. Sci.*, 2005, **578**, 108 – 123.

73 J. Sainio, M. Aronniemi, O. Pakarinen, K. Kauraala, S. Airaksinen, O. Krause and J. Lahtinen, *Appl. Surf. Sci.*, 2005, **252**, 1076 – 1083.

74 R. P. Gupta and S. K. Sen, *Phys Rev B*, 1975, **12**, 15–19.

75 M. C. Biesinger, B. P. Payne, A. P. Grosvenor, L. W. M. Lau, A. R. Gerson and R. S. C. Smart, *Appl. Surf. Sci.*, 2011, **257**, 2717 – 2730.

76 B. P. Payne, M. C. Biesinger and N. S. McIntyre, *J. Electron Spectrosc. Relat. Phenom.*, 2011, **184**, 29 – 37.

77 V. Coustet and J. Jupille, *Il Nuovo Cimento*, 1997, **19D**, 1657–1664.

78 C. Niu, K. Shepherd, D. Martini, J. Tong, J. Kelber, D. R. Jennison and A. Bogicevic, *Surf. Sci*, 2000, **465**, 163–176.

79 S. Chambers, T. Droubay, D. Jennison and T. Mattsson, *Science*, 2002, **297**, 827–831.

80 Q. Fu, T. Wagner and M. Rühle, *Surf. Sci.*, 2006, **600**, 4870–4877.

81 A. Kelber, C. Niu, K. Shepherd, D. R. Jennison and A. Bogicevic, *Surf. Sci.*, 2000, **446**, 76–88.

82 J. Jupille, *Reviews in Mineralogy & Geochemistry*, 2014, **78**, 331–369.

83 D. P. Woodruff, *Chem. Rev.*, 2013, **113**, 3863–3886.

84 R. Lazzari and I. Simonsen, *Thin Solid Films*, 2002, **419**, 124–136.